PHYSICAL REVIEW B **78**, 075317 (2008)

Gauge-invariant discretization in multiband envelope function theory and *g* factors in nanowire dots

Till Andlauer, Richard Morschl, and Peter Vogl
Walter Schottky Institut, Technische Universität München, 85748 Garching, Germany

(Received 21 February 2008; revised manuscript received 25 May 2008; published 20 August 2008)

We present a gauge-invariant discretization scheme for the multiband envelope function approximation including strain as well as relativistic effects. Our procedure is based on Wilson's formulation of gauge theories. The magnetic field couples to the envelope functions via phase factors that result from spatial discretization of the gauge covariant derivative. These phase factors contain a discretized curve integral over the vector potential. In addition, the carrier's spin couples to the magnetic field via a Zeeman term. In the case of infinitesimal grid spacings, our method becomes equivalent to the minimal substitution method. Applying our procedure, we calculate the effective electron and hole *g* tensor of InAs/InP nanowire dots and obtain excellent agreement with experimental data. We show that the correct momentum operator ordering in the Hamiltonian grossly affects the hole *g* factors. Furthermore, we investigate the influence of strain on *g* factors and nonlinear Zeeman splittings in high magnetic fields.

DOI: 10.1103/PhysRevB.78.075317 PACS number(s): 71.18.+y, 71.70.Ej, 73.21.La, 75.75.+a

I. INTRODUCTION

Solving the Schrödinger equation in a constant magnetic field within the standard minimal-coupling scheme is surprisingly problematic for a confined electronic system. Since the vector potential increases linearly with dimension, it is largest at the boundaries where the wave function is usually assumed to vanish and supposed to be no longer physically relevant. This leads to a pronounced gauge dependence of the eigenfunctions and eigenvalues that is often missed or ignored. On the other hand, magnetic-field related properties such as gyromagnetic factors are essential for controlling the spin degree of freedom of confined carriers in the area of spintronics or quantum computation.[1] Effective *g* factors have been investigated in quantum wells,[2–6] quantum wires,[7] and quantum dots[8–13] and show a strong dependence on the spatial extension, strain, and material composition of the system. It is obviously crucial to develop methods that guarantee manifestly gauge-invariant magnetic-field related solutions of the Schrödinger equation.

Surprisingly few theoretical nonperturbative approaches have been developed so far that focus on mesoscopic semiconductor nanostructures in magnetic fields.[14–28] There are atomistic approaches such as the empirical tight-binding method, where electromagnetic fields can be taken into account via a Peierls-type phase factor[29] in the transfer-matrix elements[14–22] and pseudopotential methods, where magnetic fields can be incorporated via a magnetic pseudopotential.[23–25] Recently, an *ab initio* method[26] has been developed to incorporate magnetic fields rigorously. Unfortunately, the latter approaches are practicable only for few-atom systems or crystalline systems with a few dozen atoms per unit-cell due to the numerical effort involved.

The envelope function approximation (EFA) (Refs. 30–41) is the method of choice for handling strained semiconductor structures, including relativistic effects, which extend over hundreds of nanometers. However, most approaches that incorporate magnetic fields within the framework of the EFA treat magnetic fields perturbatively.[42–44] These approaches typically hold only for subtesla magnetic fields in nanostructures; for a quantum dot of 50 nm diameter, for example, the magnetic length becomes comparable to its size already at 0.3 T. Commonly, the envelope function equation is spatially discretized for the calculation of realistic semiconductor devices. Unfortunately, applying discretization schemes to the minimal-coupling Hamiltonian breaks the gauge invariance of the discretized equations,[27] and the spectrum depends on the particular gauge choice of the vector potential. Recently, a nonperturbative eight-band EFA method has been developed that is similar to the one presented here.[28] It is also based on the gauge-invariant Wilson loop method.[45] While the details of the method are not specified in the paper, we have been able to reproduce the results in Fig. 2 of Ref. 28 by using an arithmetically averaged symmetrized operator ordering rather than the correct ordering of differential operators that has been established in Refs. 37–41. The very purpose of the present paper is to provide a general, consistent, and rigorous derivation of the method for arbitrary EFA models.

In this paper, we develop a manifestly gauge-invariant nonperturbative discretization scheme for the multiband EFA in arbitrary magnetic fields that includes relativistic effects and strain and does not contain any field-dependent fitting parameters. It is based on the concept of gauge covariant derivatives that have been developed in the context of lattice gauge theories originally.[45,46] We present a complete and concise derivation for the general multiband EFA that includes all derivatives up to second order and thoroughly accounts for their correct placement. For the case of a single band without spin-orbit interaction, the results of the present method are identical to those of the scheme developed in Ref. 27. For the general multiband case, however, a proper generalization has not been developed so far. To illustrate the method, we predict the effective *g* tensor for electrons and holes in InP/InAs nanowire-based quantum dots.

While the present method yields phase factors that multiply the zero-field Hamiltonian matrix elements similar to the Peierls phase factors for the hopping matrix elements in tight-binding theory, there are important differences. First, our method assures that the Schrödinger equation reduces to the correct continuum minimal-coupling Hamiltonian in the limit of infinitesimal grid spacing. Second, the integration path consists of unambiguous straight-line segments. In tight binding, on the other hand, the integration paths directly connect two atomic sites[18–20] of fixed distance.

The paper is organized as follows. We apply Wilson's formulation of gauge theories[45,46] to continuous multiband Schrödinger equations in Sec. II. In Sec. III, we develop the gauge-invariant discretization of the multiband EFA and take into account relativistic effects and strain. In Sec. IV, we investigate the effective electron and hole g tensor of InP/InAs nanowire-based quantum dots and compare the results with experimental data.[12] Additionally, we discuss the influence of strain and high magnetic fields on g factors.

II. GAUGE INVARIANCE IN MULTIBAND SCHRÖDINGER EQUATIONS

We start our discussion with the real-space multiband envelope function Schrödinger equation in a magnetic field,[31–34]

$$\hat{\mathcal{H}}(\mathbf{x})\mathbf{F}(\mathbf{x}) = E\mathbf{F}(\mathbf{x}), \tag{1}$$

where $\mathbf{F}$ is a column vector containing the n components of the (spin-dependent) envelope wave function and

$$\hat{\mathcal{H}}(\mathbf{x}) = \sum_{ij} K_i \hat{\mathcal{H}}^{ij}(\mathbf{x}) K_j + \sum_i [\hat{\mathcal{H}}^i(\mathbf{x}) K_i + K_i \hat{\mathcal{H}}^{i\dagger}(\mathbf{x})] + \hat{\mathcal{H}}^0(\mathbf{x}) \tag{2}$$

is the $n \times n$ matrix of the Hamiltonian operator in the EFA. Typically, the number of included bands n for semiconductor nanostructures is eight or larger. We assume a d-dimensional structure ($d \geq 2$); the indices $i,j=1,\ldots,d$ denote the Cartesian components. The momentum operators,

$$K_i = -iD_i = -i\left[\partial_i + i\frac{e}{\hbar}A_i(\mathbf{x})\right], \tag{3}$$

can be expressed in terms of the gauge covariant derivatives D_i, and A_i are the Cartesian components of the vector potential. The Hamiltonian matrix $\hat{\mathcal{H}}(\mathbf{x})$ has been decomposed into $n \times n$ matrices $\hat{\mathcal{H}}^{ij}$ that contain material-dependent $\mathbf{k}\cdot\mathbf{p}$ parameters and are second order in the operators K_i, whereas $\hat{\mathcal{H}}^i$ and $\hat{\mathcal{H}}^0$ results from the first and zeroth order terms, respectively. We will refer to these matrices by $\hat{\mathcal{H}}^\gamma$, where the index $\gamma \in \{0,i,ij\}$. The coupling of the carrier's spin to the magnetic field is included via a Zeeman term that contributes to $\hat{\mathcal{H}}^0$. A concrete implementation of $\hat{\mathcal{H}}(\mathbf{x})$ is given in Appendix A. The matrix $\hat{\mathcal{H}}^0$ is Hermitian by itself, whereas the individual second-order matrices $\hat{\mathcal{H}}^{ij}$ only obey the relation $\hat{\mathcal{H}}^{ij} = (\hat{\mathcal{H}}^{ji})^\dagger$ which suffices to guarantee $\hat{\mathcal{H}}$ to be Hermitian. We have used the ordering of the differential operators with respect to the material matrices proposed in Refs. 37–41 that avoid unphysical and spurious solutions of the EFA in heterostructures.

It can easily be shown that Eq. (1) is invariant under the gauge transformation,

$$\mathbf{F}(\mathbf{x}) \to \mathbf{F}'(\mathbf{x}) = e^{-\mathrm{i}(e/\hbar)\Lambda(\mathbf{x})}\mathbf{F}(\mathbf{x}), \tag{4}$$

$$A_i(\mathbf{x}) \to A_i'(\mathbf{x}) = A_i(\mathbf{x}) + \partial_i \Lambda(\mathbf{x}), \tag{5}$$

since $\hat{\mathcal{H}}$ contains only the covariant derivatives D_i and the magnetic-field components B_i. Importantly, it is possible to rewrite the derivatives D_i from Eq. (3) into a particular form where the vector potential only enters via a phase factor. To this end, we form the limit[45,46]

$$D_i\mathbf{F}(\mathbf{x}) = \lim_{\varepsilon\to 0}\frac{1}{\varepsilon}[U(\mathbf{x}+\boldsymbol{\varepsilon}_i,\mathbf{x})\mathbf{F}(\mathbf{x}+\boldsymbol{\varepsilon}_i) - U(\mathbf{x},\mathbf{x})\mathbf{F}(\mathbf{x})], \tag{6}$$

with $\boldsymbol{\varepsilon}_i \equiv \varepsilon\hat{\mathbf{e}}_i$ and $\hat{\mathbf{e}}_i$ denoting the unit vector pointing along the i direction. We define the so-called connection U,

$$U(\mathbf{x}+\boldsymbol{\varepsilon}_i,\mathbf{x}) = \exp\left[i\frac{e}{\hbar}\int_{\mathbf{x}}^{\mathbf{x}+\boldsymbol{\varepsilon}_i}\mathbf{A}(\mathbf{x}')d\mathbf{x}'\right], \tag{7}$$

with the integration path being a straight line from $\mathbf{x}$ to $\mathbf{x}+\boldsymbol{\varepsilon}_i$. Indeed, by inserting Eq. (7) into Eq. (6), we immediately regain Eq. (3). Note that $U(\mathbf{x},\mathbf{x})=1$. We would like to point out that an illustrative discussion of this continuum limit from a tight-binding perspective has been given in Ref. 19.

III. GAUGE-INVARIANT DISCRETIZATION

A. Prerequisites

Next, we will develop a gauge-invariant spatial discretization for the multiband Schrödinger equation [Eq. (1)]. We assume, without loss of generality, the spatial grid to be uniform,[47] to be rectangular, and to be oriented parallel to the Cartesian axes. In addition, we assume the space to be d dimensional generally and enumerate every grid point by a d-dimensional tuple $\mathbf{m}$ of integers.

First, we discretize Eq. (1) for the unproblematic case of a vanishing vector potential $\mathbf{A}=0$ using a finite difference or box discretization scheme. For example, we may approximate the derivatives ∂_i in Eq. (2) by forward finite differences,

$$\partial_i\mathbf{F}(\mathbf{x}) \to \delta_i\mathbf{F}(\mathbf{m}), \tag{8}$$

$$\delta_i\mathbf{F}(\mathbf{m}) = \frac{1}{\varepsilon}[\mathbf{F}(\mathbf{m}+\boldsymbol{\varepsilon}_i) - \mathbf{F}(\mathbf{m})], \tag{9}$$

where the vector $\boldsymbol{\varepsilon}_i \equiv \varepsilon\hat{\mathbf{e}}_i$ points to the nearest neighbor in the positive Cartesian i direction and $\varepsilon > 0$. Thus, the discretization of Eq. (1) will result in the eigenvalue problem,

$$\sum_{\mathbf{n}} \hat{\mathcal{H}}_0(\mathbf{m},\mathbf{n})\mathbf{F}(\mathbf{n}) = E\mathbf{F}(\mathbf{m}), \tag{10}$$

where the sum over $\mathbf{n}$ runs over all grid points. Here, $\hat{\mathcal{H}}_0(\mathbf{m},\mathbf{n})$ are the components of the discretized zero-field Hamiltonian operator and $\mathbf{F}(\mathbf{n})$ denotes the discretized envelope function. The dimension of the Hamiltonian matrix is the product of the total number of grid points times the number of included bands n. For simplicity, we only take into account nearest-neighbor interactions. Since the Hamiltonian includes first and second derivatives, however, the matrix elements $\hat{\mathcal{H}}_0(\mathbf{m},\mathbf{n})$ are nonzero both for the $2d$ nearest as well as for the $2d(d-1)$ diagonally adjacent (next-nearest) neighbors. The detailed values of $\hat{\mathcal{H}}_0(\mathbf{m},\mathbf{n})$ obviously depend on the chosen discretization method.

We now turn to the nontrivial case of nonzero vector potential $\mathbf{A} \neq 0$. In this case, we must construct suitable discrete approximations Δ_i of the continuous gauge covariant derivatives D_i,

$$D_i\mathbf{F}(\mathbf{x}) \to \Delta_i\mathbf{F}(\mathbf{m}), \tag{11}$$

which will lead to the discrete eigenvalue problem,

$$\sum_{\mathbf{n}} \hat{\mathcal{H}}(\mathbf{m},\mathbf{n})\mathbf{F}(\mathbf{n}) = E\mathbf{F}(\mathbf{m}), \tag{12}$$

where $\hat{\mathcal{H}}(\mathbf{m},\mathbf{n})$ are the Hamiltonian matrix elements in the magnetic field. Importantly, a straightforward discretization of Eq. (3) that follows the principle of Eq. (9),

$$\Delta_i\mathbf{F}(\mathbf{m}) \overset{?}{=} \frac{1}{\varepsilon}[\mathbf{F}(\mathbf{m}+\boldsymbol{\varepsilon}_i) - \mathbf{F}(\mathbf{m})] + i\frac{e}{\hbar}A_i(\mathbf{m})\mathbf{F}(\mathbf{m}), \tag{13}$$

results in a Schrödinger equation that *cannot* be chosen to be gauge invariant on all grid points, particularly not simultaneously on positions $\mathbf{m}$ and $\mathbf{m}+\boldsymbol{\varepsilon}_i$. Consequently, such a discretization would lead to a spectrum that depends markedly on the chosen gauge for the vector potential $\mathbf{A}$.[27] We will now show how to derive a suitable discrete approximation Δ_i that leads to a manifestly covariant eigenvalue problem.

B. Theorem and corollaries

In the field-free case, we consider the discrete approximations δ_i and δ_{ij} of the first- and second-order derivatives ∂_i and $\partial_i\partial_j$, respectively, which can be written in the following general form:

$$\delta_i\mathbf{F}(\mathbf{m}) = \frac{1}{\varepsilon}\sum_{s_i} C_i(s_i)\mathbf{F}(\mathbf{m}+s_i\boldsymbol{\varepsilon}_i),$$

$$\delta_{ii}\mathbf{F}(\mathbf{m}) = \frac{1}{\varepsilon^2}\sum_{s_i} C_{ii}(s_i)\mathbf{F}(\mathbf{m}+s_i\boldsymbol{\varepsilon}_i),$$

$$\delta_{ij}\mathbf{F}(\mathbf{m}) = \frac{1}{\varepsilon^2}\sum_{s_i,s_j} C_{ij}(s_i,s_j)\mathbf{F}(\mathbf{m}+s_i\boldsymbol{\varepsilon}_i+s_j\boldsymbol{\varepsilon}_j), \tag{14}$$

where $i \neq j$ and $s_i, s_j \in \{0, \pm 1\}$, so that the sums run over the grid point $\mathbf{m}$ and its neighbors. The coefficients C have to be chosen in such a way that they guarantee the limits $(i,j=1,\ldots,d)$,

$$\lim_{\varepsilon\to 0} \delta_i\mathbf{F}(\mathbf{m}) = \partial_i\mathbf{F}(\mathbf{x}), \tag{15}$$

$$\lim_{\varepsilon\to 0} \delta_{ij}\mathbf{F}(\mathbf{m}) = \partial_i\partial_j\mathbf{F}(\mathbf{x}). \tag{16}$$

Concretely, we have used the following values for the discretization coefficients in the applications that we will present in Sec. IV:

$$C_i(1) = 1, \quad C_i(0) = -1, \quad C_i(-1) = 0,$$

$$C_{ii}(0) = -2, \quad C_{ii}(\pm 1) = 1, \quad C_{ij}(s_i,s_j) = \frac{1}{4}s_is_j. \tag{17}$$

Additionally, we may split the matrix elements $\hat{\mathcal{H}}_0(\mathbf{m},\mathbf{n})$ of the discretized field-free Hamiltonian in Eq. (10) into their contributions corresponding to the zeroth, first, and second derivates $\hat{\mathcal{H}}^\gamma$ in Eq. (2),

$$\hat{\mathcal{H}}_0(\mathbf{m},\mathbf{n}) = \sum_{\gamma} \hat{\mathcal{H}}_0(\mathbf{m},\mathbf{n},\gamma), \tag{18}$$

with $\gamma \in \{0, i, ij\}$.

Definition. We define the discrete first-order approximation Δ_i of the gauge covariant derivative D_i and the second-order approximations Δ_{ii} and Δ_{ij} of D_i^2 and D_iD_j, respectively, by multiplying each term in Eq. (14) by the discrete connection $U(\mathbf{m},\mathbf{n},\gamma)$,

$$\Delta_i\mathbf{F}(\mathbf{m}) = \frac{1}{\varepsilon}\sum_{s_i} C_i(s_i)U(\mathbf{m},\mathbf{m}+s_i\boldsymbol{\varepsilon}_i,i)\mathbf{F}(\mathbf{m}+s_i\boldsymbol{\varepsilon}_i),$$

$$\Delta_{ii}\mathbf{F}(\mathbf{m}) = \frac{1}{\varepsilon^2}\sum_{s_i} C_{ii}(s_i)U(\mathbf{m},\mathbf{m}+s_i\boldsymbol{\varepsilon}_i,i)\mathbf{F}(\mathbf{m}+s_i\boldsymbol{\varepsilon}_i),$$

$$\begin{aligned}\Delta_{ij}\mathbf{F}(\mathbf{m}) = \frac{1}{\varepsilon^2}\sum_{s_i,s_j} C_{ij}(s_i,s_j)[&U(\mathbf{m},\mathbf{m}+s_i\boldsymbol{\varepsilon}_i+s_j\boldsymbol{\varepsilon}_j,ij)\\ &\times\mathbf{F}(\mathbf{m}+s_i\boldsymbol{\varepsilon}_i+s_j\boldsymbol{\varepsilon}_j)],\end{aligned} \tag{19}$$

where the last line holds for $i \neq j$. The discrete connection U is defined by

$$U(\mathbf{m},\mathbf{n},\gamma) = \exp\left[i\frac{e}{\hbar}\int_{S(\mathbf{m},\mathbf{n},\gamma)} \mathbf{A}(\mathbf{x}')d\mathbf{x}'\right], \tag{20}$$

where the trajectory $S(\mathbf{m},\mathbf{n},\gamma)$ starts at position $\mathbf{m}$ and ends at one of the nearest- or next-nearest-neighbor points $\mathbf{n}$. The specifier γ labels the concrete straight-line segments along the Cartesian axes i,j of a particular trajectory as follows:

$$\begin{aligned}\gamma = i, &\quad \text{path:} \quad \mathbf{m} \to \mathbf{m} \pm \boldsymbol{\varepsilon}_i = \mathbf{n},\\ \gamma = ij, &\quad \text{path:} \quad \mathbf{m} \to \mathbf{m} \pm \boldsymbol{\varepsilon}_i = \mathbf{l} \to \mathbf{l} \pm \boldsymbol{\varepsilon}_j = \mathbf{n} \quad (i \neq j),\\ \gamma^\dagger = ji, &\quad \text{path:} \quad \mathbf{m} \to \mathbf{m} \pm \boldsymbol{\varepsilon}_j = \mathbf{l}' \to \mathbf{l}' \pm \boldsymbol{\varepsilon}_i = \mathbf{n} \quad (i \neq j).\end{aligned} \tag{21}$$

Here, each segment $\boldsymbol{\varepsilon}_i$ connects only nearest neighbors as indicated in Fig. 1. The choice of this integration path guarantees that the canonical momenta obey the well-known commutator relation for finite magnetic fields. As we will show below, this requires that the trajectories associated with

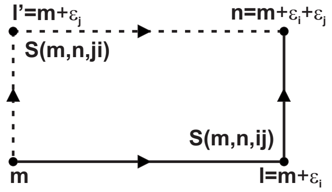

FIG. 1. Alternative integration paths in the discretization of mixed second-order derivatives.

$\gamma=ij$ and $\gamma^\dagger=ji$, respectively, enclose an area ε^2 that is compatible with the discretization stencil.

Theorem. The expressions [Eq. (19)] guarantee the correct continuum limits,

$$\lim_{\varepsilon\to 0} \Delta_i \mathbf{F}(\mathbf{m}) = D_i \mathbf{F}(\mathbf{x}), \tag{22}$$

$$\lim_{\varepsilon\to 0} \Delta_{ij} \mathbf{F}(\mathbf{m}) = D_i D_j \mathbf{F}(\mathbf{x}). \tag{23}$$

Note that one has $D_i D_j \neq D_j D_i$ for $i \neq j$.

Corollary 1. The matrix elements of the discretized Hamiltonian $\hat{H}$ for nonzero vector potential $\mathbf{A}\neq 0$ can be written in the form

$$\hat{\mathcal{H}}(\mathbf{m},\mathbf{n},\gamma) = \hat{\mathcal{H}}_0(\mathbf{m},\mathbf{n},\gamma)U(\mathbf{m},\mathbf{n},\gamma), \tag{24}$$

$$U(\mathbf{m},\mathbf{m},\gamma) = U(\mathbf{m},\mathbf{m}) = 1, \tag{25}$$

so that the discretized Schrödinger equation [Eq. (12)] reads

$$\sum_{\mathbf{n},\gamma} \hat{\mathcal{H}}_0(\mathbf{m},\mathbf{n},\gamma)U(\mathbf{m},\mathbf{n},\gamma)\mathbf{F}(\mathbf{n}) = E\mathbf{F}(\mathbf{m}). \tag{26}$$

Corollary 2. The discrete connection [Eq. (20)] obeys the following condition:

$$U^*(\mathbf{n},\mathbf{m},\gamma^\dagger) = U(\mathbf{m},\mathbf{n},\gamma), \tag{27}$$

which guarantees the Hermiticity of the Hamiltonian $\hat{H}$.

Corollary 3. The discrete connection [Eq. (20)] obeys the following discrete gauge transformation:

$$\begin{aligned} U(\mathbf{m},\mathbf{n},\gamma) &\rightarrow U'(\mathbf{m},\mathbf{n},\gamma) \\ &= \exp\left[-i\frac{e}{\hbar}\Lambda(\mathbf{m})\right]U(\mathbf{m},\mathbf{n},\gamma)\exp\left[i\frac{e}{\hbar}\Lambda(\mathbf{n})\right], \end{aligned} \tag{28}$$

which guarantees the gauge invariance of the Hamiltonian $\hat{H}$.

Corollary 4. The covariant derivatives fulfill the well-known commutator relations in the continuum limit,

$$\lim_{\varepsilon\to 0}[\Delta_x,\Delta_y] = [D_x,D_y] = i\frac{e}{\hbar}B_z, \tag{29}$$

and cyclic permutations.

C. Proofs

To prove the theorem, we first evaluate the connections U explicitly. For each path segment ε_i connecting the neighbors $\mathbf{m}$, $\mathbf{n}$ via a path specified by γ, we determine the curve integral in Eq. (20) by the trapezoidal rule,

$$\begin{aligned} \int_{S(\mathbf{m},m+\boldsymbol{\varepsilon}_i,i)} \mathbf{A}(\mathbf{x}')d\mathbf{x}' &= \frac{1}{2}[A_i(\mathbf{m})+A_i(\mathbf{m}+\boldsymbol{\varepsilon}_i)]\varepsilon \\ &\equiv \bar{A}_i(\mathbf{m}+\boldsymbol{\varepsilon}_i/2)\varepsilon. \end{aligned} \tag{30}$$

In the case of nearest neighbors $\mathbf{m}$ and $\mathbf{m}+s_i\boldsymbol{\varepsilon}_i$ ($s_i=\pm 1$), this results in the connection

$$U(\mathbf{m},\mathbf{m}+s_i\boldsymbol{\varepsilon}_i,i) = \exp\left[s_i i\frac{e}{\hbar}\bar{A}_i(\mathbf{m}+s_i\boldsymbol{\varepsilon}_i/2)\varepsilon\right]. \tag{31}$$

For the paths connecting next-nearest neighbors, specified by $\gamma=ij$, we add up the individual straight-line components of the curve integral. With the definition [Eq. (20)], this leads to

$$\begin{aligned} &U(\mathbf{m},\mathbf{m}+s_i\boldsymbol{\varepsilon}_i+s_j\boldsymbol{\varepsilon}_j,ij) \\ &\quad= \exp\left[s_i i\frac{e}{\hbar}\bar{A}_i(\mathbf{m}+s_i\boldsymbol{\varepsilon}_i/2)\varepsilon + s_j i\frac{e}{\hbar}\bar{A}_j(\mathbf{m}+s_i\boldsymbol{\varepsilon}_i+s_j\boldsymbol{\varepsilon}_j/2)\varepsilon\right], \end{aligned} \tag{32}$$

with s_i, $s_j \in \{\pm 1\}$. To show that the discretized Schrödinger equation tends to the continuum case in the limit of $\varepsilon\to 0$, we expand the connections U into powers of ε,

$$U(\mathbf{m},\mathbf{m}+s_i\boldsymbol{\varepsilon}_i,i) = 1 + s_i i\frac{e}{\hbar}A_i(\mathbf{m})\varepsilon + \mathcal{O}(\varepsilon^2). \tag{33}$$

For the wave functions $\mathbf{F}$, we have

$$\mathbf{F}(\mathbf{m}+s_i\boldsymbol{\varepsilon}_i) = \mathbf{F}(\mathbf{m}) + s_i\partial_i\mathbf{F}(\mathbf{m})\varepsilon + \mathcal{O}(\varepsilon^2). \tag{34}$$

By inserting these relations into the first derivatives [Eq. (19)], we obtain

$$\begin{aligned} \Delta_i\mathbf{F}(\mathbf{m}) = \frac{1}{\varepsilon}\sum_{s_i} C_i(s_i)\Bigg[&\mathbf{F}(\mathbf{m}) + s_i\partial_i\mathbf{F}(\mathbf{m})\varepsilon \\ &+ s_i i\frac{e}{\hbar}A_i(\mathbf{m})\mathbf{F}(\mathbf{m})\varepsilon\Bigg] + \mathcal{O}(\varepsilon). \end{aligned} \tag{35}$$

Since, the first line in Eq. (35) must reduce to the partial derivative $\partial_i\mathbf{F}(\mathbf{m})$, the coefficients C_i have to fulfill the relations

$$\sum_{s_i} C_i(s_i) = 0, \quad \sum_{s_i} C_i(s_i)s_i = 1. \tag{36}$$

This can be used to simplify the second line in Eq. (35) and leads to the required limit,

$$\Delta_i\mathbf{F}(\mathbf{m}) = \partial_i\mathbf{F}(\mathbf{m}) + i\frac{e}{\hbar}A_i(\mathbf{m})\mathbf{F}(\mathbf{m}) + \mathcal{O}(\varepsilon). \tag{37}$$

By following arguments along these lines for the second derivatives as well, we finally obtain (see Appendix B for a detailed derivation)

$$\Delta_{ij}\mathbf{F}(\mathbf{m}) = \left[\partial_i + i\frac{e}{\hbar}A_i(\mathbf{m})\right]\left[\partial_j + i\frac{e}{\hbar}A_j(\mathbf{m})\right]\mathbf{F}(\mathbf{m}) + \mathcal{O}(\varepsilon), \tag{38}$$

which has the correct continuum limit.

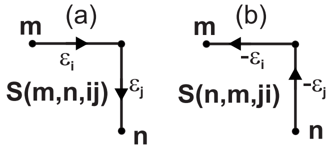

FIG. 2. Illustration of the integration paths associated with (a) the connection $U(\mathbf{m},\mathbf{n},ij)$ and (b) its Hermitian conjugate $U(\mathbf{n},\mathbf{m},ji)$.

Next, we will prove Corollary 1. This result follows from the fact that each zero-field Hamiltonian matrix element $\hat{H}_0(\mathbf{m},\mathbf{n},\gamma)$ gets augmented by a corresponding phase factor $U(\mathbf{m},\mathbf{n},\gamma)$, $\gamma\in\{0,i,ij\}$, according to Eq. (19). In order to prove Corollary 2, we need to show that the Hamiltonian $\hat{H}$ is Hermitian. This implies the relation

$$U^*(\mathbf{n},\mathbf{m},\gamma^\dagger)\hat{H}_0^\dagger(\mathbf{n},\mathbf{m},\gamma^\dagger) = \hat{H}^\dagger(\mathbf{n},\mathbf{m},\gamma^\dagger) \equiv \hat{H}(\mathbf{m},\mathbf{n},\gamma) = \hat{H}_0(\mathbf{m},\mathbf{n},\gamma)U(\mathbf{m},\mathbf{n},\gamma). \tag{39}$$

The field-free Hamiltonian is definitely Hermitian and obeys $\hat{H}_0^\dagger(\mathbf{n},m,\gamma^\dagger)=\hat{H}_0(\mathbf{m},\mathbf{n},\gamma)$, since $\mathcal{H}^{ij}=(\mathcal{H}^{ji})^\dagger$. Thus, we are led to the condition

$$U^*(\mathbf{n},\mathbf{m},\gamma^\dagger) = U(\mathbf{m},\mathbf{n},\gamma). \tag{40}$$

We now show that this equation is fulfilled indeed. For a nearest-neighbor connection, we immediately find this relation to hold,

$$U(\mathbf{m},\mathbf{m}+\boldsymbol{\varepsilon}_i,i) = \exp\left[-i\frac{e}{\hbar}\int_{S(\mathbf{m}+\boldsymbol{\varepsilon}_i,\mathbf{m},i)}\mathbf{A}(\mathbf{x}')d\mathbf{x}'\right] = U^*(\mathbf{m}+\boldsymbol{\varepsilon}_i,\mathbf{m},i). \tag{41}$$

For the next-nearest-neighbor connection between $\mathbf{m}$ and $\mathbf{n}=\mathbf{m}+\boldsymbol{\varepsilon}_i+\boldsymbol{\varepsilon}_j$ specified by $\gamma=ij$, we obtain

$$\begin{aligned}U(\mathbf{m},\mathbf{n},ij) &= \exp\left[i\frac{e}{\hbar}\bar{A}_i(\mathbf{m}+\boldsymbol{\varepsilon}_i/2)\varepsilon + i\frac{e}{\hbar}\bar{A}_j(\mathbf{m}+\boldsymbol{\varepsilon}_i+\boldsymbol{\varepsilon}_j/2)\varepsilon\right]\\ &= \exp\left[-i\frac{e}{\hbar}\bar{A}_j(\mathbf{n}-\boldsymbol{\varepsilon}_j/2)\varepsilon - i\frac{e}{\hbar}\bar{A}_i(\mathbf{n}-\boldsymbol{\varepsilon}_j-\boldsymbol{\varepsilon}_i/2)\varepsilon\right]^*\\ &= U^*(\mathbf{n},\mathbf{m},ji),\end{aligned} \tag{42}$$

which is precisely the condition [Eq. (40)]. Note that the appropriate paths $S(\mathbf{m},\mathbf{n},ij)$ and $S(\mathbf{n},\mathbf{m},ji)$ contain the same segments but are traversed in the opposite direction (see Fig. 2).

We now turn to Corollary 3. Let us write the discretized Schrödinger equation [Eq. (26)] in a different gauge,

$$\sum_{\mathbf{n},\gamma}\hat{H}_0(\mathbf{m},\mathbf{n},\gamma)U'(\mathbf{m},\mathbf{n},\gamma)\mathbf{F}'(\mathbf{n}) = E\mathbf{F}'(\mathbf{m}). \tag{43}$$

The relation between the envelope function $F(\mathbf{n})$ and its corresponding form in the primed gauge is the same as in the continuous case and reads

$$\mathbf{F}(\mathbf{n}) \to \mathbf{F}'(\mathbf{n}) = \exp\left[-i\frac{e}{\hbar}\Lambda(\mathbf{n})\right]\mathbf{F}(\mathbf{n}). \tag{44}$$

Inserting Eq. (44) into Eq. (43) leads to the requirement that $U(\mathbf{m},\mathbf{n},\gamma)$ has to fulfill a discretized version of the continuum gauge transformation,

$$\begin{aligned}U(\mathbf{m},\mathbf{n},\gamma) &\to U'(\mathbf{m},\mathbf{n},\gamma)\\ &= \exp\left[-i\frac{e}{\hbar}\Lambda(\mathbf{m})\right]U(\mathbf{m},\mathbf{n},\gamma)\exp\left[i\frac{e}{\hbar}\Lambda(\mathbf{n})\right].\end{aligned} \tag{45}$$

We now show that this condition is fulfilled indeed. The discrete gauge transformation for Eq. (30) reads

$$\bar{A}_i'(\mathbf{m}+\boldsymbol{\varepsilon}_i/2) = \bar{A}_i(\mathbf{m}+\boldsymbol{\varepsilon}_i/2) + \frac{1}{\varepsilon}[\Lambda(\mathbf{m}+\boldsymbol{\varepsilon}_i)-\Lambda(\mathbf{m})]. \tag{46}$$

Inserting this expression into the nearest-neighbor connection [Eq. (31)], we immediately obtain Eq. (45). For the connections to next-nearest neighbors, we get

$$\begin{aligned}&U'(\mathbf{m},\mathbf{m}+\boldsymbol{\varepsilon}_i+\boldsymbol{\varepsilon}_j,ij)\\ &= \exp\left\{i\frac{e}{\hbar}[\bar{A}_i(\mathbf{m}+\boldsymbol{\varepsilon}_i/2)\varepsilon + \Lambda(\mathbf{m}+\boldsymbol{\varepsilon}_i)-\Lambda(\mathbf{m})]\right\}\\ &\quad\times\exp\left\{i\frac{e}{\hbar}[\bar{A}_j(\mathbf{m}+\boldsymbol{\varepsilon}_i+\boldsymbol{\varepsilon}_j/2)\varepsilon + \Lambda(\mathbf{m}+\boldsymbol{\varepsilon}_i+\boldsymbol{\varepsilon}_j)\right.\\ &\quad\left.-\Lambda(\mathbf{m}+\boldsymbol{\varepsilon}_i)]\right\},\end{aligned} \tag{47}$$

$$\begin{aligned}&=\exp\left[-i\frac{e}{\hbar}\Lambda(\mathbf{m})\right]U(\mathbf{m},\mathbf{m}+\boldsymbol{\varepsilon}_i+\boldsymbol{\varepsilon}_j,ij)\\ &\quad\times\exp\left[i\frac{e}{\hbar}\Lambda(\mathbf{m}+\boldsymbol{\varepsilon}_i+\boldsymbol{\varepsilon}_j)\right],\end{aligned} \tag{48}$$

which confirms Eq. (45) as well. In addition, the discrete gauge transformation [Eq. (46)] obviously has the correct continuum limit [Eq. (5)]. Together, these results confirm that the discretized Schrödinger equation [Eq. (26)] is invariant under local phase transformations. Finally, we prove Corollary 4. Using Eq. (38), we can see that the discretized covariant derivatives obey the commutator relation [Eq. (29)] in the continuum limit,

$$\lim_{\varepsilon\to 0}[\Delta_i,\Delta_j] = \lim_{\varepsilon\to 0}\left[i\frac{e}{\hbar}(\partial_i A_j - \partial_j A_i) + \mathcal{O}(\varepsilon)\right] = i\frac{e}{\hbar}\mathrm{sgn}(i,j,k)B_k = [D_i,D_j]. \tag{49}$$

An issue we have not discussed so far concerns the uniqueness of the integration trajectory $S(\mathbf{m},\mathbf{n},\gamma)$. For connections between nearest neighbors, the integration path is unique. For diagonally adjacent neighbors, however, there are two possible paths to choose from (see Fig. 1). Gauge invariance only demands that the integration path continuously connects position $\mathbf{m}$ with position $\mathbf{n}$. The Hermiticity of H is guaranteed once the same path is traversed in opposite direction for

$H^\dagger$ (see Fig. 2). In addition, however, the covariant derivatives have to fulfill the commutator relations [Eq. (29)]. For the second-order approximations Δ_{ij} in Eq. (19), the only element that depends on the order of i and j is the path characterized by $\gamma = ij$, since $C_{ij} = C_{ji}$. Thus, we can see that it is the precise choice of γ in Eq. (21) that guarantees the correct order in Eq. (38) which in turn guarantees the validity of Corollary 4. This additional constraint causes the integration trajectory to be unique.

D. Summary of method

We have developed a general method to include a magnetic field into the multiband envelope function Schrödinger equation in a gauge-invariant manner. We have shown that the resulting Hamiltonian is Hermitian, guarantees the correct continuum limit, and preserves the correct operator ordering.

To apply this method, one first discretizes Hamiltonian (2) in the field-free Schrödinger equation [Eq. (1)] using the discretization scheme of Eq. (14) with the coefficients [Eq. (17)]. This yields the discretized Schrödinger equation [Eq. (10)] with the Hamiltonian matrix consisting of the zeroth-, first-, and second-order derivatives [Eq. (18)]. Next, each matrix element of the Hamiltonian $\hat{H}_0(\mathbf{m}, \mathbf{n}, \gamma)$ is to be multiplied by the phase factor $U(\mathbf{m}, \mathbf{n}, \gamma)$ in order to take into account the vector potential $\mathbf{A}$. For nearest neighbors, this phase factor is given by Eq. (31). For diagonally adjacent neighbors, Eq. (32) is needed. In the latter case, one must be careful to discriminate terms of the form $\gamma = ij$ from those that contain $\gamma = ji$. Finally, one needs to add a zeroth-order derivative term, the Zeeman term, namely (see Appendix A), to the Hamiltonian in order to include the coupling of the carrier's spin to the magnetic field.

IV. RESULTS: EFFECTIVE *g* FACTORS OF QUANTUM WIRE DOTS

A. Electron *g* tensor

As a first illustration of the present method, we predict the effective g tensor of electrons in nanowire-based quantum dots. Experimentally, effective electron g factors of InP/InAs nanowire dots have been determined recently.[12] The quantum dots possess the wurtzite crystal structure, have a hexagonal shape, and are characterized by a diameter D, the InAs quantum dot length L, and a left and right InP barrier thickness w (see Fig. 3). The diameter D equals 50 nm in these experiments. The experimental values of the effective g factors range from $|g^*| = 13$ which is close to the InAs bulk value for dots with $L = 270$ nm to $|g^*| = 2.3$ for the thinnest dots with $L = 8$ nm.

Electron g factors for these quantum dots have been calculated previously.[48] However, we found the hole g factors in Fig. 2 of the related Ref. 28 to disagree with the present method. We can quantitatively reproduce the results of this paper by using an incorrectly symmetrized ordering that can be obtained by substituting Eq. (51) into Eq. (A3). In order to show consistently calculated results for both electron and holes in terms of the present scheme, we present here also briefly the results for electron g factors.

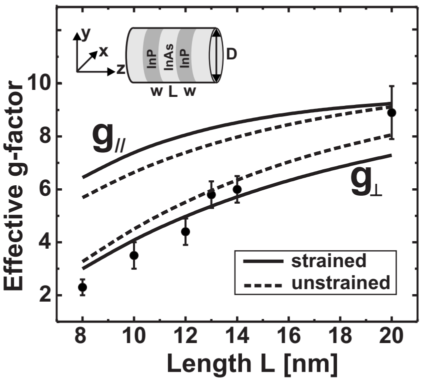

FIG. 3. Comparison of calculated strained (solid lines), calculated unstrained (dashed lines), and experimental (circles) effective electron g factors for wire dots of length L. The $g_\parallel$ and $g_\perp$ components correspond to the magnetic-field lying parallel and perpendicular to the wire axis, respectively. Experimentally, only the $g_\perp$ components have been determined (Ref. 12).

In our calculations, we have simplified the geometry by assuming a quadratic or circular cross section of the dots (see inset of Fig. 3), since the precise shape of the dots does not influence our results in the range of the studied dot dimensions and magnetic fields. The $\mathbf{k} \cdot \mathbf{p}$ parameters for InAs and InP have been taken for the zinc-blende structure from Ref. 49 except for the κ parameter that has been tabulated in Ref. 50. The spin splitting $\Delta E_{\uparrow\downarrow} = E^{\uparrow} - E^{\downarrow}$ of the electron ground state in the dot has been calculated within a relativistic eight-band $\mathbf{k} \cdot \mathbf{p}$ model that is detailed in Appendix A. The effective g tensor elements G^{kl} $(k, l = 1, 2, 3)$ can then be extracted from the relation

$$\Delta E_{\uparrow\downarrow} = \mu_B \sqrt{\sum_{kl} B_k G^{kl} B_l}, \qquad (50)$$

where B_i are the Cartesian components of the magnetic field. The spin splitting must be evaluated for a sufficiently small value of $|B|$ (which we took to be equal to 0.1 T) to exclude higher order contributions. Due to symmetry, only fields along the (100) and (001) directions need to be considered in the present case for solving the linear system of equations that result from Eq. (50). For our geometry and within the eight-band $\mathbf{k} \cdot \mathbf{p}$ model, we have $G^{xx} = G^{yy}$ and $G^{ij} = 0$ for all off-diagonal tensor components. We have determined the signs of the g tensor elements from the spin directions of the Zeeman split states and found that all calculated g factors had negative sign $(E^{\uparrow} < E^{\downarrow})$ as expected from the bulk values.

Figure 3 compares the calculated perpendicular electron g factor $g_\perp = (G^{xx})^{1/2}$ with the experimental results of Ref. 12 for dot lengths L between 8 and 20 nm and a barrier thickness of $w = 6$ nm. Furthermore, our calculations predict the electron g factor for the magnetic field parallel to the wire axis, $g_\parallel = (G^{zz})^{1/2}$. The theory takes into account the strain as we will discuss in more detail below; Fig. 3 shows both type of results where strain effects in the Hamiltonian have been included or (artificially) set to zero to elucidate the sole

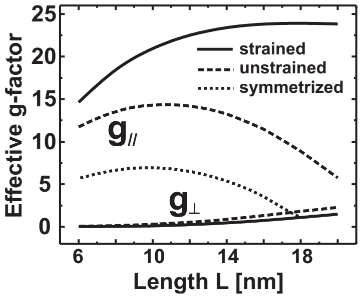

FIG. 4. Comparison of calculated strained (solid lines) and unstrained (dashed lines) effective hole g factors for wire dots of length L and magnetic-fields pointing perpendicular ($g_\perp$) and parallel ($g_\parallel$) to the wire axis. The dotted line illustrates the importance of the correct operator ordering in Eq. (A3) by showing the unstrained $g_\parallel$ for a Hermitian but naively and therefore incorrectly symmetrized Hamiltonian.

strain effect on the g factor. As one can deduce from the figure, our calculations excellently reproduce the experimentally observed trend that shows the g factors to increase with increasing dot length. We have checked that the use of the correct operator ordering in Eq. (A3) plays a negligible role for the electron g factors in the nanowire dots. Thus, our results are consistent with Ref. 48.

B. Hole g tensor

We now turn to the hole g factors in these nanowire-based quantum dots. For quantum wells in a magnetic field, each valence subband splits into a complicated pattern of Landau levels that are conventionally labeled by the Bloch function orbital momentum J_z and an integer $n=-2,-1,0,\cdots$.[51] Since all those states with the same modulus $|J_z|$ become degenerate for zero magnetic field, these states tend to cross at some magnetic field which makes it nontrivial to uniquely define hole g factors. The situation in quantum dots is far more transparent. Here, the lateral confinement splits the states corresponding to different lateral momenta of the envelope function already at $B=0$. This allows one to uniquely define the hole g tensor by the energy separation between the energetically lowest dot state and the lowest excited state with reversed sign of J_z. For the dots considered in the present paper, this pair of states is dominantly heavy-hole-like and originates from the pair of quantum well Landau levels with $J_z=-3/2$, $n=-2$ and $J_z=3/2$, $n=1$.[51] These states remain the energetically lowest dot states up to magnetic fields of 4 T and ensure an unambiguous definition of the hole g factor.

In Fig. 4, we show our calculated results for different dot lengths, both with and without the inclusion of strain, and for parallel and perpendicular magnetic fields. Again, all g factors are negative, but for simplicity we only discuss their absolute values. The size dependence of hole g factors in quantum dots is more complicated than for electrons. The dots considered here have a large width to height ratio so that carriers are only weakly confined laterally, i.e., perpendicular to the wire axis. Therefore, the calculated hole g factors in Fig. 4 resemble the values found for wide quantum wells, which can be obtained from the bulk Hamiltonian.[31] In the latter case, already a six-band $\mathbf{k}\cdot\mathbf{p}$ model gives the well-known results[2,21,44] $g_\parallel^{\mathrm{hh}}=6\kappa$, $g_\parallel^{\mathrm{lh}}=2\kappa$, $g_\perp^{\mathrm{hh}}=0$, $g_\perp^{\mathrm{lh}}=4\kappa$, where κ is a Luttinger parameter. For InAs, one has $\kappa=7.68$ which is much larger than this constant in InP, where one has $\kappa=0.97$.[50] Due to the confinement, the wire dot ground state is mainly heavy-hole-like and its g factors $g_\parallel, g_\perp$ show an anisotropy that is somewhat smaller but still of the order of the bulk anisotropy. For the shortest dots, the wave functions penetrate into the InP barriers. This effect leads to a reduction in the g factors because κ is smaller for InP. Furthermore, the orbital motion is hampered in the limit $L\rightarrow 0$ so that the hole g factors tend toward the pure spin value in this limit. The larger the dot length L and the more extended the hole wave functions are, on the other hand, the closer the g factors lie to the bulk values of InAs. However, there is a competing effect that turns out to dominate in the limit of large values of L. The reduction in axial confinement for large L implies an increase in the light-hole (lh) contribution of the ground state. Indeed, the light hole contribution amounts to only 1.5% for $L=8$ nm but increases to 12.0% for $L=20$ nm. Since $g_\perp^{\mathrm{lh}} > g_\perp^{\mathrm{hh}}$ in bulk, $g_\perp$ increases also in dots in the limit of large L. Analogously, $g_\parallel$ decreases in this limit since $g_\parallel^{\mathrm{lh}} < g_\parallel^{\mathrm{hh}}$ in bulk. Qualitatively similar trends have been predicted previously for self-assembled Si/Ge quantum dots[21] and for InGaAs dots.[11,22] Experimentally, heavy-hole (hh) g factors have been determined for GaAs quantum wells[2,3,5] and for self-assembled InGaAs dots.[8,9] In both of these situations, the observed values are much smaller than for InAs nanowire dots, since the bulk g factors of GaAs are much smaller ($\kappa=1.2$), and carriers are significantly more strongly confined in self-assembled dots.

Finally, we have investigated the influence of the momentum operator ordering in Hamiltonian (A3) on hole g factors. As discussed in detail in Appendix A, the known continuum limit of the $\mathbf{k}\cdot\mathbf{p}$ Hamiltonian[31] imposes an unambiguous constraint on the ordering of momentum operators in the discrete Hamiltonian.[39,41] To investigate the effect of this operator ordering, we have replaced the correct Hamiltonian in Eq. (A3) by an incorrect one, namely, a naively symmetrized version. To this end we set [see Eq. (A3)]

$$N'_+ = N_- = (N'_+ + N_-)/2. \tag{51}$$

The resulting hole $g_\parallel$ factors for quantum wire dots are included in Fig. 4 (dotted line) and are seen to deviate strongly from the correctly calculated values. We have repeated this calculation for the experimentally determined hole g factor in Ref. 8 and found excellent agreement with the present theory, when we invoke the correct operator ordering.

C. Strain effects on electron and hole g tensor

The InP/InAs nanowires investigated by Björk *et al.*[12] are freestanding wires with a relaxed InAs lattice structure and pseudomorphically strained InP layers. We have calculated the spatial strain profile of the heterostructure wires by minimizing the total elastic energy in a linear continuum elasticity model.[52,53] Figure 5(a) shows the resulting strain profile along the wire axis near the dot with a length of $L=20$ nm and barrier thicknesses of $w=6$ nm. We find the InAs dot to

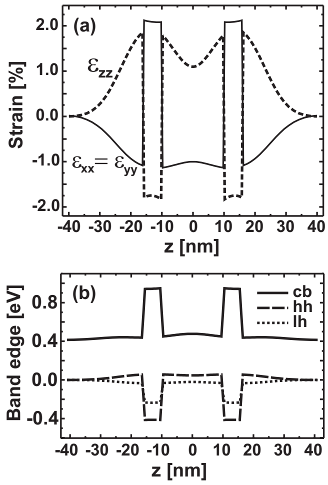

FIG. 5. (a) Cross section of calculated strain components along the wire axis z for a dot with a length of $L=20$ nm and a barrier thickness of $w=6$ nm. (b) Calculated energies of conduction band (cb), heavy hole (hh), and light hole (lh) valence-band edges.

be compressively strained ($\varepsilon_{xx}=\varepsilon_{yy}<0$), whereas the InP barriers show a tensile strain. Outside of the InP barrier material, the lattice relaxes to unstrained InAs after approximately 25 nm. Our calculations are qualitatively consistent with previous experimental and theoretical strain results obtained for similar wires with much smaller diameters and a single InAs/InP interface.[54] The incorporation of this strain into the Hamiltonian via linear deformation potentials (see Appendix A) leads to changes in the electronic structure and the g factors. For the electron g factor, these trends can already be understood in a bulk model originally derived for electrons in homogeneously strained layers.[55] The band gap within the dot is slightly increased due to the hydrostatic pressure component of the strain, $\delta E_g=(a_c-a_v)(\varepsilon_{xx}+\varepsilon_{yy}+\varepsilon_{zz})>0$, and the heavy-hole band edge gets pushed above the light-hole band edge due to a tetragonal distortion that is proportional to $\varepsilon_{zz}-\varepsilon_{xx}$ [see Fig. 5(b)]. This distortion additionally induces a mixing of the light hole and the split-off (so) hole band. Together, these changes in the electronic structure affect the coupling between conduction and valence bands and enhance the anisotropy of the electron g factor.[55] Namely, the increased band gap reduces the conduction-band–valence-band coupling, which is the source for the deviation of the electron g factors from 2. For the perpendicular g factor, the lh/so mixing adds up to this effect. Therefore $g_\perp$ is decreased, still reproducing the experimental results. By contrast, for $g_\parallel$, the lh/so mixing has an increasing effect. Here the hh/lh splitting additionally raises the g factor. Together, these effects exceed the general reduction due to the increased band gap and lead to larger values of $g_\parallel$.

Hole g factors are far more sensitive to strain effects because the hole states are p states and couple directly to the spin. The main effect of the compressive strain within the dot is to shift the heavy-hole band edge above the light-hole band edge. This reduces the light-hole contribution to the ground state from 1.5% in the unstrained case to 1.1% for $L=8$ nm and from 12% to 3.8% for $L=20$ nm. Again following the trends in the bulk values, this implies a slight increase in $g_\perp$ and a decrease in $g_\parallel$ that is much less pronounced than in the unstrained case. This explains the increasing difference between the strained and unstrained g factors in the limit of large dot lengths L.

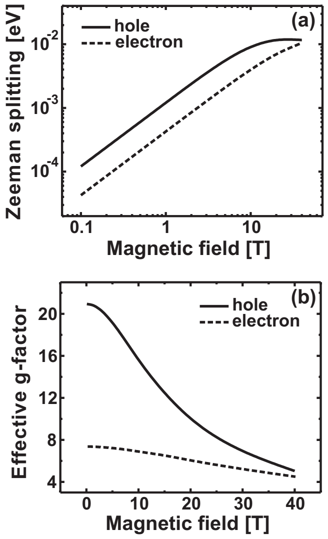

FIG. 6. (a) Calculated electron (dashed lines) and hole (solid lines) Zeeman splittings and (b) effective g factors for electrons and holes as a function of the magnetic-field lying parallel to the wire axis for a dot of length $L=10$ nm.

D. Spin splitting for high magnetic fields

Since our approach takes into account magnetic fields nonperturbatively, we may study the electronic structure at high magnetic fields B. In the framework of $\mathbf{k}\cdot\mathbf{p}$ theory, however, the magnetic length must remain large compared to the lattice constant. The strong confinement and strain induced light- and heavy-hole splittings guarantee that all light-hole states remain energetically well separated from the heavy-hole ground state up to the highest B fields considered, so that the hole g factor remains unambiguously defined. The spin splitting of the lowest electron state increases linearly with B up to 10 T for a dot of length $L=10$ nm and the magnetic-field pointing along the wire axis. The spin splitting of the hole ground-state responds more sensitively to B and deviates from linearity already at 4 T. In Fig. 6, we depict the electron and hole $g_\parallel$ factor up to 40 T. We see that the effective $g_\parallel$ factors $\Delta E_{\uparrow\downarrow}/(\mu_B B)$ decrease with increasing field strength, which resembles the experimentally observed trends in quantum wells.[3,4] We associate this effect with a magnetic-field induced band mixing. For the hole ground state, we find the average heavy-hole component of the spin-up and spin-down states to decrease with increasing B. This diminishes the $g_\parallel$ factor of holes as has been pointed out previously.[22] We find an analogous but less pronounced behavior for electrons, where the conduction-band component decreases with increasing B.

To visualize the influence of high magnetic fields, in Fig. 7, we show the lateral deformation of the electron ground-state wave function within an $L=20$ nm dot as a function of

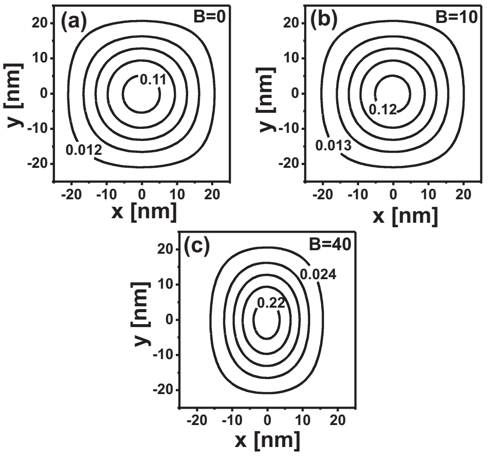

FIG. 7. Cross section of the density of the electron ground state at the dot center in units of 10^{18} cm^{-3} for different magnetic fields in tesla. The density of the ground state shows a noticeable deformation if the ratio $\alpha=\hbar\omega_c/\Delta E$ is close to one. (a) $\alpha=0$, (b) $\alpha=0.2$, and (c) $\alpha=0.8$.

a magnetic field $B_\perp$ perpendicular to the wire axis. This wave-function deformation is controlled by the ratio between the magnetic cyclotron energy $\hbar\omega_c$ and the lowest zero-field electron excitation energy ΔE in the dot. The latter quantity is a measure of the confinement. The larger the value of ΔE, the smaller the deformation induced by the magnetic field is,[28] and this can be clearly deduced from the figure.

V. SUMMARY

In summary, we have developed a general method to solve the multiband Schrödinger equation in an external potential plus a magnetic field in an efficient and manifestly gauge-invariant manner. It is based on the concept of gauge covariant derivatives.[45,46] The phase factors comprise a discretized form of the curve integral over the vector potential. The integration paths are compatible with the discretization grid and are given by a chain of straight-line path segments connecting nearest neighbors. Their choice is uniquely defined by the constraint that the momentum operators must obey well-known commutator relations. The Hamiltonian matrix elements are shown to be gauge invariant for any finite grid spacing and converge to the same correct continuum result in the limit of infinitesimal grid spacing. The coupling of the carrier's spin to the magnetic field is properly taken into account by a Zeeman term within the EFA scheme.

To illustrate the method, we have computed the effective g tensor for electrons and holes in InP/InAs nanowire-based quantum dots. For electrons, we obtained excellent agreement with experimental data.[12] Our results show that the changes in the electron g factors correlate well with the spatial extent of the wave functions and therefore with the angular motion, as has been argued before.[28] The g factors for holes are shown to depend much more sensitively on the sample geometry and material composition which allows significant tailoring of their values, e.g., by changing the dot size. We predict a strong anisotropy of the g tensor components for magnetic fields that lie parallel or perpendicular to the wire axis. We find this anisotropy to get enhanced with strain. Additionally, we have calculated the influence of high magnetic fields on the g factors and find markedly nonlinear Zeeman splittings.

ACKNOWLEDGMENTS

The authors acknowledge support from the Deutsche Forschungsgemeinschaft (Grants No. SFB 631 and No. SPP 1285), the Austrian Science Fund FWF (SFB IRON), and the Nanosystems Initiative Munich (NIM).

APPENDIX A

We have based our calculations in Sec. IV on the following eight-band $\mathbf{k}\cdot\mathbf{p}$ envelope function Hamiltonian in real space.[32,33] In the basis of spin-resolved zone-center conduction and valence-band Bloch functions $|q\sigma\rangle \in \{s,x,y,z\}\times\{\uparrow,\downarrow\}$, the Hamiltonian for zero magnetic field can be written in the following form:[39,41]

$$\mathcal{H}^{8\times8}(\mathbf{k}) = \begin{pmatrix} \mathcal{H}^{4\times4}(\mathbf{k}) + \mathcal{H}_\varepsilon^{4\times4} & 0 \\ 0 & \mathcal{H}^{4\times4}(\mathbf{k}) + \mathcal{H}_\varepsilon^{4\times4} \end{pmatrix} + \mathcal{H}_{so}^{8\times8}. \tag{A1}$$

Here, the Hamiltonian $\mathcal{H}^{4\times4}(\mathbf{k})$ contains the momentum operator $\mathbf{k}=-i\nabla$ and material parameters that are spatially dependent in nanostructures,

$$\mathcal{H}^{4\times4}(\mathbf{k}) = \begin{pmatrix} E_c + \sum_{i=1}^{3} k_i A_c k_i & iPk_1 & iPk_2 & iPk_3 \\ -ik_1P & & & \\ -ik_2P & & \mathcal{H}_{vv}^{3\times3} & \\ -ik_3P & & & \end{pmatrix}, \tag{A2}$$

$$\mathcal{H}_{vv}^{3\times3}(\mathbf{k}) = E_v + \frac{\hbar^2}{2m_0}\sum_{i=1}^{3} k_i^2 + \begin{pmatrix} k_1L'k_1 + \sum_{i=2,3} k_iMk_i & k_1N'_+k_2 + k_2N_-k_1 & k_1N'_+k_3 + k_3N_-k_1 \\ k_1N_-k_2 + k_2N'_+k_1 & k_2L'k_2 + \sum_{i=1,3} k_iMk_i & k_2N'_+k_3 + k_3N_-k_2 \\ k_1N_-k_3 + k_3N'_+k_1 & k_2N_-k_3 + k_3N'_+k_2 & k_3L'k_3 + \sum_{i=1,2} k_iMk_i \end{pmatrix}. \tag{A3}$$

Here, A_c includes the free-electron mass and remote-band contributions to the conduction-band mass.[41] P denotes the interband coupling matrix element. Instead of the original linearly independent Dresselhaus parameters[56] F, G, H_1, and H_2, we have specified this Hamiltonian in terms of the more commonly used derived Dresselhaus parameters L, M, N_+, and N_-, which are related to each other by

$$L = F + 2G, \quad M = H_1 + H_2, \tag{A4}$$

$$N_+ = F - G, \quad N_- = H_1 - H_2. \tag{A5}$$

The latter two parameters have been introduced in Ref. 41. Another commonly used and tabulated set of derived Luttinger parameters[31,50,57] is γ_1, γ_2, γ_3, and κ. In terms of these parameters, we can write

$$L = \frac{\hbar^2}{2m_0}(-\gamma_1 - 4\gamma_2 - 1), \tag{A6}$$

$$M = \frac{\hbar^2}{2m_0}(-\gamma_1 + 2\gamma_2 - 1), \tag{A7}$$

$$N_+ = \frac{\hbar^2}{2m_0}(-3\gamma_3 - 3\kappa - 1), \tag{A8}$$

$$N_- = \frac{\hbar^2}{2m_0}(-3\gamma_3 + 3\kappa + 1). \tag{A9}$$

Since these parameters have been originally defined for a six-band $\mathbf{k}\cdot\mathbf{p}$ model,[31,56,57] two of them require a modification for the present eight-band model in order to avoid double counting of terms. The correct eight-band parameters are related to the original ones by the relation

$$L' = L + \frac{P^2}{E_g}, \quad N'_+ = N_+ + \frac{P^2}{E_g}. \tag{A10}$$

The strain field Hamiltonian $\mathcal{H}_\varepsilon^{4\times4}$ is given by

$$\mathcal{H}_\varepsilon^{4\times4} = \begin{pmatrix} a_c\,\mathrm{Tr}(\varepsilon) & 0 & 0 & 0 \\ 0 & l\varepsilon_{11} + m(\varepsilon_{22} + \varepsilon_{33}) & n\varepsilon_{12} & n\varepsilon_{13} \\ 0 & n\varepsilon_{12} & l\varepsilon_{22} + m(\varepsilon_{11} + \varepsilon_{33}) & n\varepsilon_{23} \\ 0 & n\varepsilon_{13} & n\varepsilon_{23} & l\varepsilon_{33} + m(\varepsilon_{11} + \varepsilon_{22}) \end{pmatrix}. \tag{A11}$$

Here, ε_{ij} are the components of the symmetric strain tensor, a_c denotes the absolute deformation potential of the conduction band, and the parameters l, m, and n are determined by the absolute deformation potential a_v and the shear deformation potentials b, d of the valence band,[32,33]

$$l = a_v + 2b, \tag{A12}$$

$$m = a_v - b, \tag{A13}$$

$$n = \sqrt{3}d. \tag{A14}$$

Finally, the spin-orbit Hamiltonian $\mathcal{H}_{\mathrm{so}}^{8\times8}$ contains only a few nonvanishing elements between the p-type basis functions,

$$(\mathcal{H}_{\mathrm{so}}^{8\times8})_{x\uparrow,y\uparrow} = -i\frac{\Delta_0}{3}, \quad (\mathcal{H}_{\mathrm{so}}^{8\times8})_{x\uparrow,z\downarrow} = \frac{\Delta_0}{3}, \tag{A15}$$

and cyclic permutations. Hamiltonian (A3) contains a particular ordering of the momentum operator components that has been proposed by Refs. 37–41. We now show that *this and only this* specific ordering guarantees the correct $\mathbf{k}\cdot\mathbf{p}$ Hamiltonian for bulk in nonzero magnetic fields. Magnetic fields are introduced into Hamiltonian (A3) simply by the replacement $k_i \rightarrow K_i = k_i + (e/\hbar)A_i(\mathbf{x})$. Note that the Dresselhaus[56] parameters are constants in bulk materials. Using the commutator relation for the momentum operator, we have

$$[K_i, K_j] = K_iK_j - K_jK_i = -i\frac{e}{\hbar}\,\mathrm{sgn}(i,j,k)B_k. \tag{A16}$$

Using these relations, the $\mathbf{k}\cdot\mathbf{p}$ Hamiltonian in a magnetic field now reads

$$\mathcal{H}^{3\times 3}_{vv}(\mathbf{K}) = E_v + \frac{\hbar^2}{2m_0}\sum_{i=1}^{3} K_i^2 + \begin{pmatrix} L'K_1^2 + M\sum\limits_{i=2,3} K_i^2 & N'\{K_1,K_2\} & N'\{K_1,K_3\} \\ N'\{K_1,K_2\} & L'K_2^2 + M\sum\limits_{i=1,3} K_i^2 & N'\{K_2,K_3\} \\ N'\{K_1,K_3\} & N'\{K_2,K_3\} & L'K_3^2 + M\sum\limits_{i=1,2} K_i^2 \end{pmatrix} - \mu_B(3\kappa+1)\sum_{i=1}^{3}\hat{I}^i B_i, \tag{A17}$$

where $N'=N'_{+}+N_{-}$ and we have used the anticommutator

$$\{K_i,K_j\} = \frac{1}{2}(K_iK_j + K_jK_i). \tag{A18}$$

The 3×3 angular-momentum matrices $\hat{I}^i$ have been defined by Ref. 31 and μ_B is the Bohr magneton. This result corresponds precisely to the $\mathbf{k}\cdot\mathbf{p}$ Hamiltonian in a magnetic field as proposed in Ref. 31.

Since we include the spin degree of freedom, finally we need to augment Hamiltonian (A1) by the Zeeman term,

$$\mathcal{H}^{8\times 8}_{\sigma B} = \frac{g_0\mu_B}{2}\sum_{i=1}^{3}\hat{S}^i B_i, \tag{A19}$$

where $g_0=2$ and the matrix elements of the spin matrices $\hat{S}^i$ are given in terms of the Pauli matrices $\hat{\sigma}^i$,

$$S^i_{q'\sigma',q\sigma} = \langle q'\sigma'|\hat{\sigma}^i|q\sigma\rangle = \delta_{q',q}\hat{\sigma}^i_{\sigma',\sigma}. \tag{A20}$$

This Zeeman term, together with the last term in Eq. (A17), leads to the bulk hole g tensor components noted in Sec. IV B. Finally, the Hamiltonian in Eq. (A1) can be written in the form of Eq. (2). The matrices $\hat{\mathcal{H}}^{ij}$ result from those elements of Eq. (A1) that are second order in the operators K_i, while $\hat{\mathcal{H}}^i$ results from the first-order terms. The remaining terms that are zero order in K_i contribute to the matrix $\hat{\mathcal{H}}^0$.

APPENDIX B

In order to prove Eq. (38) for $i=j$, we expand the connection U in Eq. (31) up to second order of ε,

$$U(\mathbf{m},\mathbf{m}+s_i\boldsymbol{\varepsilon}_i,i) = 1 + s_i i\frac{e}{\hbar}A_i(\mathbf{m})\varepsilon + s_i^2\frac{1}{2}i\frac{e}{\hbar}(\partial_i A_i)(\mathbf{m})\varepsilon^2 - s_i^2\frac{1}{2}\frac{e^2}{\hbar^2}A_i^2(\mathbf{m})\varepsilon^2 + \mathcal{O}(\varepsilon^3). \tag{B1}$$

For the wave functions $\mathbf{F}$, we have

$$\mathbf{F}(\mathbf{m}+s_i\boldsymbol{\varepsilon}_i) = \mathbf{F}(\mathbf{m}) + s_i\partial_i\mathbf{F}(\mathbf{m})\varepsilon + s_i^2\frac{1}{2}\partial_i^2\mathbf{F}(\mathbf{m})\varepsilon^2 + \mathcal{O}(\varepsilon^3). \tag{B2}$$

By inserting Eqs. (B1) and (B2) into Eq. (19), we get

$$\begin{aligned}\Delta_{ii}\mathbf{F}(\mathbf{m}) = \frac{1}{\varepsilon^2}\sum_{s_i} C_{ii}(s_i)\Bigg\{ & \mathbf{F}(\mathbf{m}) + s_i\partial_i\mathbf{F}(\mathbf{m})\varepsilon + s_i^2\frac{1}{2}\partial_i^2\mathbf{F}(\mathbf{m})\varepsilon^2 \\ & + s_i i\frac{e}{\hbar}A_i(\mathbf{m})\varepsilon[\mathbf{F}(\mathbf{m}) + s_i\partial_i\mathbf{F}(\mathbf{m})\varepsilon] \\ & + s_i^2\frac{1}{2}\left[i\frac{e}{\hbar}(\partial_i A_i)(\mathbf{m}) - \frac{e^2}{\hbar^2}A_i^2(\mathbf{m})\right]\mathbf{F}(\mathbf{m})\varepsilon^2\Bigg\} + \mathcal{O}(\varepsilon).\end{aligned} \tag{B3}$$

Here the sum runs over $s_i \in \{0,\pm 1\}$. The first line in Eq. (B3) must tend to $\partial_i^2\mathbf{F}(\mathbf{m})$ as in the field-free case, which requires the coefficients to obey

$$\sum_{s_i} C_{ii}(s_i) = \sum_{s_i} C_{ii}(s_i)s_i = 0, \tag{B4}$$

$$\sum_{s_i} C_{ii}(s_i)s_i^2 = 2. \tag{B5}$$

Using these relations, the entire expression [Eq. (B3)] tends toward the correct continuum limit [Eq. (38)]. For the mixed second-order derivatives, the diagonally adjacent neighbors are needed. For this case, we expand Eq. (32) analogous to Eq. (B1),

$$\begin{aligned} & U(\mathbf{m},\mathbf{m}+s_i\boldsymbol{\varepsilon}_i+s_j\boldsymbol{\varepsilon}_j,ij) \\ & = 1 + \left[s_i i\frac{e}{\hbar}A_i(\mathbf{m}) + s_j i\frac{e}{\hbar}A_j(\mathbf{m})\right]\varepsilon \\ & \quad + s_i^2\frac{1}{2}\left[i\frac{e}{\hbar}(\partial_i A_i)(\mathbf{m}) - \frac{e^2}{\hbar^2}A_i^2(\mathbf{m})\right]\varepsilon^2 \\ & \quad + s_i s_j\left[i\frac{e}{\hbar}(\partial_i A_j)(\mathbf{m}) - \frac{e^2}{\hbar^2}A_i(\mathbf{m})A_j(\mathbf{m})\right]\varepsilon^2 \\ & \quad + s_j^2\frac{1}{2}\left[i\frac{e}{\hbar}(\partial_j A_j)(\mathbf{m}) - \frac{e^2}{\hbar^2}A_j^2(\mathbf{m})\right]\varepsilon^2 + \mathcal{O}(\varepsilon^3).\end{aligned} \tag{B6}$$

Furthermore, we need

$$\begin{aligned} & \mathbf{F}(\mathbf{m}+s_i\boldsymbol{\varepsilon}_i+s_j\boldsymbol{\varepsilon}_j) \\ & = \mathbf{F}(\mathbf{m}) + [s_i\partial_i\mathbf{F}(\mathbf{m}) + s_j\partial_j\mathbf{F}(\mathbf{m})]\varepsilon \\ & \quad + \left[s_i^2\frac{1}{2}\partial_i^2\mathbf{F}(\mathbf{m}) + s_i s_j\partial_i\partial_j\mathbf{F}(\mathbf{m}) + s_j^2\frac{1}{2}\partial_j^2\mathbf{F}(\mathbf{m})\right]\varepsilon^2 \\ & \quad + \mathcal{O}(\varepsilon^3).\end{aligned} \tag{B7}$$

Inserting these relations into Eq. (19) gives ($s_i,s_j \in \{0,\pm 1\}$),

$$\Delta_{ij}\mathbf{F}(\mathbf{m}) = \frac{1}{\varepsilon^2}\sum_{s_i,s_j} C_{ij}(s_i,s_j)\Bigg\{\mathbf{F}(\mathbf{m}) + [s_i\partial_i\mathbf{F}(\mathbf{m}) + s_j\partial_j\mathbf{F}(\mathbf{m})]\varepsilon + \left[s_i^2\frac{1}{2}\partial_i^2\mathbf{F}(\mathbf{m}) + s_is_j\partial_i\partial_j\mathbf{F}(\mathbf{m}) + s_j^2\frac{1}{2}\partial_j^2\mathbf{F}(\mathbf{m})\right]\varepsilon^2$$
$$+ \left[s_i i\frac{e}{\hbar}A_i(\mathbf{m}) + s_j i\frac{e}{\hbar}A_j(\mathbf{m})\right][\mathbf{F}(\mathbf{m}) + s_i\partial_i\mathbf{F}(\mathbf{m})\varepsilon + s_j\partial_j\mathbf{F}(\mathbf{m})\varepsilon]\varepsilon + s_i^2\frac{1}{2}\left[i\frac{e}{\hbar}(\partial_iA_i)(\mathbf{m}) - \frac{e^2}{\hbar^2}A_i^2(\mathbf{m})\right]\mathbf{F}(\mathbf{m})\varepsilon^2$$
$$+ s_is_j\left[i\frac{e}{\hbar}(\partial_iA_j)(\mathbf{m}) - \frac{e^2}{\hbar^2}A_i(\mathbf{m})A_j(\mathbf{m})\right]\mathbf{F}(\mathbf{m})\varepsilon^2 + s_j^2\frac{1}{2}\left[i\frac{e}{\hbar}(\partial_jA_j)(\mathbf{m}) - \frac{e^2}{\hbar^2}A_j^2(\mathbf{m})\right]\mathbf{F}(\mathbf{m})\varepsilon^2\Bigg\} + \mathcal{O}(\varepsilon). \tag{B8}$$

Again, the field-free case constricts the coefficients to

$$\sum_{s_i,s_j} C_{ij}(s_i,s_j) = \sum_{s_i,s_j} C_{ij}(s_i,s_j)s_i = 0, \tag{B9}$$

$$\sum_{s_i,s_j} C_{ij}(s_i,s_j)s_j = 0, \tag{B10}$$

$$\sum_{s_i,s_j} C_{ij}(s_i,s_j)s_j^2 = \sum_{s_i,s_j} C_{ij}(s_i,s_j)s_i^2 = 0, \tag{B11}$$

$$\sum_{s_i,s_j} C_{ij}(s_i,s_j)s_is_j = 2. \tag{B12}$$

Inserting these relations into Eq. (B8) results in Eq. (38), which has the correct limit.

---

[1] D. Loss and D. P. DiVincenzo, Phys. Rev. A **57**, 120 (1998).

[2] H. W. van Kesteren, E. C. Cosman, W. A. J. A. van der Poel, and C. T. Foxon, Phys. Rev. B **41**, 5283 (1990).

[3] M. J. Snelling, E. Blackwood, C. J. McDonagh, R. T. Harley, and C. T. B. Foxon, Phys. Rev. B **45**, 3922 (1992).

[4] N. J. Traynor, R. T. Harley, and R. J. Warburton, Phys. Rev. B **51**, 7361 (1995).

[5] X. Marie, T. Amand, P. Le Jeune, M. Paillard, P. Renucci, L. E. Golub, V. D. Dymnikov, and E. L. Ivchenko, Phys. Rev. B **60**, 5811 (1999).

[6] A. Malinowski and R. T. Harley, Phys. Rev. B **62**, 2051 (2000).

[7] M. Oestreich, A. P. Herbele, W. W. Rühle, R. Nötzel, and K. Ploog, Europhys. Lett. **31**, 399 (1995).

[8] M. Bayer, A. Kuther, A. Forchel, A. Gorbunov, V. B. Timofeev, F. Schäfer, J. P. Reithmaier, T. L. Reinecke, and S. N. Walck, Phys. Rev. Lett. **82**, 1748 (1999).

[9] M. Bayer, O. Stern, A. Kuther, and A. Forchel, Phys. Rev. B **61**, 7273 (2000).

[10] J.-M. Meyer, I. Hapke-Wurst, U. Zeitler, R. J. Haug, and K. Pierz, Phys. Status Solidi B **224**, 685 (2001).

[11] T. Nakaoka, T. Saito, J. Tatebayashi, and Y. Arakawa, Phys. Rev. B **70**, 235337 (2004).

[12] M. T. Björk, A. Fuhrer, A. E. Hansen, M. W. Larsson, L. E. Fröberg, and L. Samuelson, Phys. Rev. B **72**, 201307(R) (2005).

[13] T. P. Mayer Alegre, F. G. G. Hernandez, A. L. C. Pereira, and G. Medeiros-Ribeiro, Phys. Rev. Lett. **97**, 236402 (2006).

[14] D. Springsguth, R. Ketzmerick, and T. Geisel, Phys. Rev. B **56**, 2036 (1997).

[15] E. Anisimovas and P. Johansson, Phys. Rev. B **60**, 7744 (1999).

[16] V. Ya. Demikhovskii, JETP Lett. **78**, 680 (2003).

[17] M. Graf and P. Vogl, Phys. Rev. B **51**, 4940 (1995).

[18] T. B. Boykin, R. C. Bowen, and G. Klimeck, Phys. Rev. B **63**, 245314 (2001).

[19] T. B. Boykin, Am. J. Phys. **69**, 793 (2001).

[20] B. A. Foreman, Phys. Rev. B **66**, 165212 (2002).

[21] A. V. Nenashev, A. V. Dvurechenskii, and A. F. Zinovieva, Phys. Rev. B **67**, 205301 (2003).

[22] W. Sheng and A. Babinski, Phys. Rev. B **75**, 033316 (2007).

[23] P. K. Misra and L. M. Roth, Phys. Rev. **177**, 1089 (1969).

[24] P. K. Misra, J. Phys. Chem. Solids **177**, 1098 (1969).

[25] N. C. Das and P. K. Misra, Phys. Rev. B **4**, 225 (1971).

[26] W. Cai and G. Galli, Phys. Rev. Lett. **92**, 186402 (2004); E. Lee, W. Cai, and G. A. Galli, J. Comput. Phys. **226**, 1310 (2007).

[27] M. Governale and C. Ungarelli, Phys. Rev. B **58**, 7816 (1998).

[28] C. E. Pryor and M. E. Flatté, Phys. Rev. Lett. **96**, 026804 (2006); **99**, 179901(E) (2007).

[29] R. Peierls, Z. Phys. **80**, 763 (1933).

[30] J. M. Luttinger and W. Kohn, Phys. Rev. **97**, 869 (1955).

[31] J. M. Luttinger, Phys. Rev. **102**, 1030 (1956).

[32] E. L. Ivchenko and G. E. Pikus, *Superlattices and Other Heterostructures: Symmetry and Optical Phenomena*, Springer Series in Solid State Sciences Vol. 110 (Springer, Heidelberg, 1997).

[33] G. L. Bir and G. E. Pikus, *Symmetry and Strain-Induced Effects in Semiconductors* (Wiley, New York, 1974).

[34] U. Rössler, *Solid State Theory* (Springer, Heidelberg, 2004).

[35] G. Bastard, Phys. Rev. B **24**, 5693 (1981).

[36] M. Altarelli, U. Ekenberg, and A. Fasolino, Phys. Rev. B **32**, 5138 (1985).

[37] M. G. Burt, J. Phys.: Condens. Matter **4**, 6651 (1992).

[38] M. G. Burt, J. Phys.: Condens. Matter **11**, 53 (1999).

[39] B. A. Foreman, Phys. Rev. B **48**, 4964 (1993).

[40] B. A. Foreman, Phys. Rev. B **54**, 1909 (1996).

[41] B. A. Foreman, Phys. Rev. B **56**, R12748 (1997).

[42] L. M. Roth, B. Lax, and S. Zwerdling, Phys. Rev. **114**, 90 (1959).

[43] A. A. Kiselev, E. L. Ivchenko, and U. Rössler, Phys. Rev. B **58**, 16353 (1998).

[44] A. A. Kiselev, K. W. Kim, and E. Yablonovitch, Phys. Rev. B **64**, 125303 (2001).

[45] I. Montvay and G. Münster, *Quantum Fields on a Lattice* (Cambridge University Press, Cambridge, England, 1997).

[46] K. Wilson, Phys. Rev. D **10**, 2445 (1974).

[47] We note that Eq. (12) becomes a generalized eigenvalue problem for nonuniform grids. However, one can apply a scale transformation that leads one back to the form of Eq. (12).

[48] A. De and C. E. Pryor, Phys. Rev. B **76**, 155321 (2007).

[49] I. Vurgaftman, J. R. Meyer, and L. R. Ram-Mohan, J. Appl. Phys. **89**, 5815 (2001).

[50] *Semiconductors: Intrinsic Properties of Group IV Elements and III-V, II-VI, and I-VII Compounds*, Landolt-Börnstein, New Series, Group III Vol. 22, Pt. A, edited by O. Madelung (Springer, Berlin, 1987).

[51] U. Ekenberg and M. Altarelli, Phys. Rev. B **32**, 3712 (1985).

[52] L. D. Landau and E. M. Lifshitz, *Theory of Elasticity* (Pergamon, Oxford, 1959).

[53] S. Hackenbuchner, in *Elektronische Struktur von Halbleiter-Nanobauelementen im thermodynamischen Nichtgleichgewicht*, Selected Topics of Semiconductor Physics and Techology Vol. 48, edited by G. Abstreiter, M.-C. Amann, M. Stutzmann, and P. Vogl (Verein zur Förderung des Walter Schottky Instituts, Garching, 2002).

[54] M. W. Larsson, J. B. Wagner, M. Wallin, P. Hakansson, L. E. Fröberg, L. Samuelson, and L. R. Wallenberg, Nanotechnology **18**, 015504 (2007).

[55] G. Hendorfer and J. Schneider, Semicond. Sci. Technol. **6**, 595 (1991).

[56] G. Dresselhaus, A. F. Kip, and C. Kittel, Phys. Rev. **98**, 368 (1955).

[57] P. Lawaetz, Phys. Rev. B **4**, 3460 (1971).